arXiv:1408.0896v2 [astro-ph.SR] 13 Nov 2014

A method for computing synchrotron and inverse-Compton emission from hydrodynamic simulations of supernova remnants

M. Obergaulinger[a,*], J.M[a] Chimeno Hernández[a], P. Mimica[a], M.Á Aloy Torás[a], A. Iyudin[b,c]

[a] *Departament d´Astronomia i Astrofísica, Universitat de València, Edifici d´Investigació Jeroni Munyoz, C/ Dr. Moliner, 50, E-46100 Burjassot (València), Spain*

[b] *Extreme Universe Laboratory, Skobeltsyn Institute of Nuclear Physics, Moscow State University by M.V. Lomonosov, Leninskie Gory, 119991 Moscow, Russian Federation*

[c] *Max-Planck-Institut für Extraterrestrische Physik, Postfach 1312 D-85741 Garching, Bavaria, Germany*

Abstract

The observational signature of supernova remnants (SNRs) is very complex, in terms of both their geometrical shape and their spectral properties, dominated by non-thermal synchrotron and inverse-Compton scattering. We propose a post-processing method to analyse the broad-band emission of SNRs based on three-dimensional hydrodynamical simulations. From the hydrodynamical data, we estimate the distribution of non-thermal electrons accelerated at the shock wave and follow the subsequent evolution as they lose or gain energy by adiabatic expansion or compression and emit energy by radiation. As a first test case, we use a simulation of a bipolar supernova expanding into a cloudy medium. We find that our method qualitatively reproduces the main observational features of typical SNRs and produces fluxes that agree with observations to within a factor of a few. allowing for further use in more extended sets of models.

Keywords: Supernova remnants; shock waves; non-thermal emission

1. Introduction

Supernova remnants (SNRs) are characterised by electromagnetic emission across a wide spectral range, which is generated by several different emission mechanisms such as (thermal) bremsstrahlung, synchrotron and inverse

*Corresponding author

Email addresses: martin.obergaulinger@uv.es (M. Obergaulinger), jochiher@alumni.uv.es (J.M[a] Chimeno Hernández), petar.mimica@uv.es (P. Mimica), miguel.a.aloy@uv.es (M.Á Aloy Torás), aiyudin@srd.sinp.msu.ru (A. Iyudin)

Compton scattering (IC), and the line emission of many different chemical elements in various ionisation levels (see, e.g., Gould, 1965; de Jager and Harding, 1992). Similar processes play an important role in many other astrophysical objects (e.g., Zdziarski, 1986). Consequently, the spectra and lightcurves depend on many physical processes, some of which can be–within a broad range of uncertainties–inferred from observational data (explosion energy, properties of the environment. Unfortunately, there are other key processes which may be not fully understood such as the physics of radiative shocks and the associated particle acceleration. Furthermore, many SNRs show a complex geometry with deviations from spherical symmetry that may be attributed to combinations of asymmetries in the explosion, instabilities during the propagation of the shock wave such as Rayleigh-Taylor, Vishniac (thin shell) or unstable cooling (see, e.g., Chevalier and Imamura, 1982), inhomogeneities in the surrounding interstellar medium (ISM), or magnetic fields. For a review on observations of SNRs, we refer to Reynolds (2008). Among the galactic remnants, SNR RX J0852.0-4622 (Vela Jr.) is a particularly interesting case, with observations from radio to TeV energies revealing a complex emission geometry (Duncan and Green, 2000; Slane et al., 2001; Aharonian et al., 2007; Iyudin et al., 2007; Tanaka et al., 2011; Kishishita et al., 2013).

The complexity of the radiation processes and the hydrodynamics of the SNR restrict a straightforward interpretation of observations and require the use of increasingly complex models in order to understand the physics of SNRs in general and of individual objects. Depending on the objective, models may focus on different effects, while making simplification in other sectors of physics. For instance, Obergaulinger et al. (2014) performed a series of three-dimensional simulations of the expansion of supernova blast waves into a clumpy environment (for models of simular settings, see Orlando et al., 2005, 2006). Paying attention in particular to the case of Vela Jr., they concentrated their efforts on an accurate modelling of the hydrodynamics of the interaction between the shock wave and clouds in the ISM. Their model for the electromagnetic emission, on the other hand, was relatively limited and accounted only for thermal bremsstrahlung, leaving out some of the most important contributions to the emission coming from SNRs.

Our goal now is to remedy this limitation by modelling the non-thermal emission of the simulated SNRs. To this end, we propose a method for post-processing the existing simulations. We assume that particle acceleration at the shock wave generates a population of high-energy electrons that subsequently cool by synchrotron and inverse-Compton radiation. The advantage of our approach is that it can provide and quick estimate of the non-thermal emission, but at a cost of several simplifications w.r.t., e.g. the spectra of the shock-accelerated electrons, the seed photons for IC, and the magnetic field in the SNR. Furthermore, we neglect ionisation and line emission. Kishishita et al. (2013) used similar methods to interpret observations of the Vela Jr. SNR, but coupled the emission model to spherically symmetric analytic hydrodynamical models, whereas we will use self-consistent hydrodynamical simulations to determine the evolution of the shock wave. Our method is, however, less accurate

than, e.g. the simulations of Lee et al. (2013), which couple hydrodynamics, non-equilibrium ionisation, non-linear diffuse shock acceleration, and cosmic-ray production in a fully self-consistent manner. We also refer to the work of Orlando et al. (2011) for computations of the non-thermal emission in SNRs based on multi-dimensional simulations. We additionally note that our approach is at an approximate level related to the relativistic emission modelling of Mimica et al. (2004) and Mimica et al. (2010). By virtue of its simplicity, the method lends itself easily to an investigation of the impact of variation of the input physics, e.g. of the spectra of accelerated electrons or the seed photons for the IC process.

We will begin the presentation in this article with a brief recap of the hydrodynamical simulations of Obergaulinger et al. (2014) and an outline of our emission model in Sect. 2, then present results for the non-thermal radiation emitted by one of the models (Sect. 3), before summarising the main results and drawing further conclusions in Sect. 4.

2. Physical ingredients and numerical method

Following the implementation in the SPEV code outlined in Mimica et al. (2009), we model the evolution of a population of non-thermal electrons accelerated by the shock wave and their subsequent emission of synchrotron and IC radiation using the post-processing algorithm *SPEVita* based on three-dimensional hydrodynamic simulations. Such a two-step approach requires that the radiative energy losses do not significantly alter the structure and evolution of the remnant. This condition is satisfied in our cases because the total amount of energy carried away by photons is small w.r.t. the total kinetic and internal energy of the remnant.

We furthermore work in the limit of low optical depth of the gas in the SNR. This assumption is justified by the low gas density. If we estimate the optical depth of the SNR using the Thomson scattering cross section, $\sigma_{\mathrm{Th}} = 0.66 \times 10^{-24}\,\mathrm{cm}^2$, we find that even the densest clouds in our simulations (densities up to $1000\,\mathrm{cm}^{-3}$, size up to 10 pc) have optical depths of less than 0.01, and most of the gas is much more optically thin. This fact allows us to directly obtain the radiation arriving at an observer location from the emissivity at the source location instead of solving the much more complex equations of radiative transfer. Furthermore, we neglect synchrotron self-absorption since it is unimportant in the frequencies considered here (above the optical band).

Hydrodynamical models. From the simulations of Obergaulinger et al. (2014), we select a model (model `S25A`) in which a bipolar supernova explosion ejects a mass of $M_{\mathrm{SN}} = 6M_{\odot}$ with a total explosion energy of $E_{\mathrm{SN}} = 6.7 \times 10^{51}$ erg into an ISM of particle density $n_{\mathrm{ISM}} = 0.25\,\mathrm{cm}^{-3}$ and temperature $T_{\mathrm{ISM}} = 10$ K. The ISM contains four large high-density clouds placed in the NW, N, SE and S directions from the the centre of the explosion at positions where X-ray bright features are suggestive of an interaction between the shock wave and overdense structures in the ISM.

The expanding shock wave roughly maintains its initial bipolar shape with an interior consisting of a hot, tenuous gas with very little substructure. This changes once, after a time of about $t \sim 700\,\mathrm{yr}$, the interaction between the shock wave and the clouds channels the expanding gas between the gas clouds and enhances the mixing of post-shock fluid elements. On the time scales under consideration here, i.e. up to 1500 years after the explosion, the clouds are not disrupted by the shock, but experience considerable deformation and, most importantly, heating of the shocked surfaces, which, as a combination of high temperature and high density, show up as prominent emitters of thermal radiation.

Non-thermal emission. The passage of the shock wave across a fluid element generates a population of relativistic non-thermal electrons. Without modelling the acceleration process in detail, we assume that the 0^{th} moment of the distribution function of the electrons, $n^0(\gamma)$, i.e. the number density of particles per unit Lorentz factor, γ, follows a power-law distribution,

$$n^0(\gamma) = n_0^0 \left(\frac{\gamma}{\gamma_{\mathrm{min}}}\right)^{-q} \text{ for } \gamma_{\mathrm{min}} \leq \gamma \leq \gamma_{\mathrm{max}}. \tag{1}$$

For further reference, we note that the Lorentz factor is related to the particle momentum and energy via the electron mass, m_e, as $p = \gamma m_e v$ ($p = \gamma m_e c$ for the case of ultrarelativistic electrons considered in the following) and $e = \gamma m_e c^2$, respectively. Aside from the power-law index q, there are three *free* parameters that specify the electron energy distribution, namely, the minimum and maximum Lorentz factors, γ_{min} and γ_{max}, and the normalisation n_0^0. The following conditions allow us to fix these three parameters:

1. We first estimate the value of the stochastic magnetic field energy density generated at shocks assuming that it is a fraction, ϵ_b, of the thermal energy density, u_S (provided by our hydrodynamic models), i.e., $B = \sqrt{8\pi\epsilon_b u_S}$.
2. Following Reynolds (2008), we relate the cut-off energy of the electron distribution to the magnetic field strength at the site of acceleration (computed in point 1, above), $E_{\mathrm{max}} = 100\,\mathrm{TeV}\ \alpha_{\mathrm{acc}} \left(\frac{B}{1\,\mu\mathrm{G}}\right)^{-1/2}$, and thus, we shall specify the value of the parameter α_{acc}.
3. Given γ_{max}, the normalisation n_0^0 and the minimum Lorentz factor are direct functions of the efficiency of the acceleration process, i.e. the fraction of electrons accelerated in the shock wave and the fraction of total energy they carry, ϵ_n and ϵ_e, respectively.

In practise, we ignore all electrons below $\gamma_{\mathrm{min;emi}} = 10$ when computing synchrotron and IC emission to be consistent with the approximations we will employ in their respective emissivities.

We consider only a single episode of particle acceleration. Upon passage of the shock wave across one of our tracer particles, we define a momentum grid of n_p zones distributed logarithmically spanning the range $[p_{\mathrm{min}}, p_{\mathrm{max}}] = [\gamma_{\mathrm{min}}, \gamma_{\mathrm{max}}] \times m_e c$ and initialise $n^0(p_i), i = 1, ..., n_p$ according to Eq. (1).

Afterwards, the electrons suffer radiative losses and gain or lose energy due to adiabatic compression or expansion, respectively. In the evolution equation for the 0^{th} moment,

$$D_t \ln n^0 + \left(-\frac{p}{3}\Theta + \mathcal{B}\right) \partial_p \ln n^0 = -\frac{2}{3}\Theta - \partial_p \mathcal{B}, \tag{2}$$

these effects are accounted for by the expansion coefficient

$$\Theta = -D_t \ln \rho \tag{3}$$

and the emission coefficient

$$\mathcal{B} = -\frac{4\sigma_{\mathrm{T}}(u_B + u_{\mathrm{ph}})}{3m_e^2 c^2} p^2. \tag{4}$$

Here, D denotes the Lagrangian time derivative, ρ is the gas density, and σ_{T} is the Thomson cross section. The emission coefficient is the sum of a synchrotron contribution, proportional to the magnetic energy density $u_B = \vec{B}^2/2$, and an IC contribution, proportional to the energy density of the background photon field, u_{ph}. u_B and u_{ph} are, besides the efficiencies determining the initial distribution of non-thermal particles, the most important free parameters of our analysis.

The formal solution of Eq. (2), given by Mimica et al. (2009), lends itself straightforwardly to a discretisation on a time-dependent grid in momentum space. Given the momentum of an electron $p(t_0)$ at time t_0 and setting

$$\frac{\rho(t_1)}{\rho(t_0)} = \exp\left(3k_{\mathrm{a}}\delta t\right) \tag{5}$$

and

$$\mathcal{B} = -k_{\mathrm{e}}\delta t, \tag{6}$$

we find the Lorentz factor of electrons at time $t_1 = t_0 + \delta t$ as a function of their Lorentz factor at time t_0

$$\gamma(t_1) = \gamma(t_0)\frac{k_{\mathrm{a}} \exp\left(k_{\mathrm{a}}\delta t\right)}{k_{\mathrm{a}} + p(t_0)(\exp\left(k_{\mathrm{a}}\delta t\right) - 1)}, \tag{7}$$

and the 0^{th} moment as

$$n^0(t_1) = n^0(t_0)\left[\exp\left(k_{\mathrm{a}}\delta t\right)\left(1 + \gamma(t_0)\frac{k_{\mathrm{a}}}{k_{\mathrm{e}}}(\exp\left(k_{\mathrm{a}}\delta t\right) - 1)\right)\right]^2. \tag{8}$$

Solving Eqns. 7 and 8 for each tracer particle that already passed by the shock wave, we obtain the time evolution of the distribution of non-thermal particles at discrete momentum values $p_i(t)$. Between these interface values, we approximate the function $n^0(\gamma)$ by piecewise power laws of index q, i.e.

$$n^0(\gamma) = n_i^0 \left(\frac{\gamma}{\gamma_i}\right)^{-q} \text{ for } \gamma_i \leq \gamma < \gamma_{i+1}. \tag{9}$$

This procedure does not directly yield the spectral distribution of the emitted radiation, which we compute in an additional step using the expressions summarised by Böttcher and Reimer (2012). The synchrotron emission at frequency ν of non-thermal electrons is described by the emissivity coefficient, i.e. the energy emitted per unit volume, unit frequency interval, and unit time

$$j^{\mathrm{syn}}(\nu) = \frac{1}{4\pi} \int \mathrm{d}\gamma \, n(\gamma) P_\nu(\gamma). \tag{10}$$

The radiative output of the distribution of electrons can be computed by integrating the product of the single-particle emission function,

$$P_\nu(\gamma) = \frac{32c}{9\Gamma(4/3)} \left(\frac{q_e^2}{m_e c^2} \right)^2 u_B \gamma^2 \frac{\nu^{1/3}}{\nu_{\mathrm{c}}^{4/3}} \exp\left(-\nu/\nu_{\mathrm{c}}\right), \tag{11}$$

and the power-law distribution Eq. (9) over Lorentz factor. The critical frequency ν_c is given by $\nu_{\mathrm{c}} = \frac{3 q_e B}{2 m_e c^2} \gamma^2$ (q_e is the electron charge). For IC, we restrict ourselves to the simple case of a mono-energetic seed field of photons of frequency ν_0, leading to an emission coefficient for the power-law spectrum of electrons with momentum $p_i \leq \gamma m_e c < p_{i+1}$ approximately given by

$$j_i^{\mathrm{IC}}(\nu) = C \left(\frac{\nu}{\nu_{\mathrm{c}}} \right)^2 \left\{ \left[\max\left(\gamma_i, \frac{h\nu}{m_e c^2}, \sqrt{\frac{\nu}{2\nu_{\mathrm{c}}}} \right) \right]^{-q-3} - \gamma_{i+1}^{-q-3} \right\} \tag{12}$$

if $\gamma_{i+1} \geq \max\left(\frac{h\nu}{m_e c^2}, \sqrt{\frac{\nu}{2\nu_0}} \right)$ and $j_\nu^{\mathrm{IC}} = 0$ otherwise; the normalisation is given in terms of the number density of seed photons, $n_{\mathrm{ph},0}$, by $C = \frac{hc\sigma_{\mathrm{T}} n_i^0 n_{\mathrm{ph},0}}{8\pi(q+3)\gamma_i^{-q}}$.

For each tracer particle and its non-thermal electron distribution, we evaluate the emission coefficients at discrete frequencies between infrared and TeV energies. We determine emission maps, i.e. the total spectral emissivity $J_\nu(x, y; T)$ arriving at the position of an observer at distance D along the $z-$axis from gas at position (x, y) on the celestial plane by integrating the emissivity along the trajectory of a ray of light at time T,

$$J_\nu^{\mathrm{syn;IC}}(x, y; T) = \int_{-\infty}^{D} \mathrm{d}z \, j_\nu^{\mathrm{syn;IC}}(x, y, z; t = T - \frac{1}{c}(D - z)). \tag{13}$$

For the spatial integration, we take into account the expansion of the gas by assuming that each tracer particle represents a uniform distribution of electrons centred at its position and with a volume $V(t) = V(t_0)\frac{\rho(t)}{\rho(t_0)}$, where $V(t_0)$ denotes the volume assigned to the particle at the start of the simulation. Finally, an integration of $J_\nu(x, y; T)$ over x and y yields the total, spatially unresolved emission of the gas.

3. Results

Keeping the hydrodynamical model fixed, we computed several model light curves, spectra, and emission maps. The goal of this series of models is not

Model	$\alpha_{\rm acc}$	ϵ_e	ϵ_n	ϵ_b	Linestyle (Colour)
Reference	0.1	0.3	0.14	10^{-3}	Solid (black)
1	0.01	0.3	0.14	10^{-3}	Triple dot-dash (blue)
2	1	0.3	0.14	10^{-3}	Dashed (blue)
3	0.1	0.09	0.14	10^{-3}	Triple dot-dash (green)
4	0.1	0.45	0.14	10^{-3}	Dashed (green)
5	0.1	0.3	0.042	10^{-3}	Triple dot-dash (red)
6	0.1	0.3	0.21	10^{-3}	Dashed (red)
7	0.1	0.3	0.14	10^{-4}	Triple dot-dash (orange)
8	0.1	0.3	0.14	10^{-2}	Dashed (orange)

Table 1: List of our models. For each model (name or number in the first column), we list the parameter $\alpha_{\rm acc}$ governing the acceleration efficiency, the normalisations of the energy and number densities of the non-thermal electrons (ϵ_e and ϵ_n), and the magnetisation parameter, ϵ_b. The last column gives the linestyle and colour used for the spectrum of the corresponding model in Fig. 3.

first and foremost to provide a good fit to the observations of a particular SNR, but to assess in principle the viability of our model to reproduce the most important features of the non-thermal emission from SNRs and to explore the dependence of the results on the input physics and the free parameters governing the evolution of the non-thermal electrons and their emission, viz. the efficiency of particle acceleration, the magnetic field in the SNR, and the background photon field acting as seed for IC scattering. To facilitate our goal, we will qualitatively compare the models to the observations of the Vela Jr. SNR in radio (Duncan and Green, 2000), X-ray (*ASCA* GIS, Aharonian et al., 2007), *Fermi*-LAT (Tanaka et al., 2011), and *HESS* (Aharonian et al., 2007). We defer a more rigorous comparison with observational data to an upcoming study.

We investigate how the emission depends on four parameters, viz. $\alpha_{\rm acc}$, ϵ_e, ϵ_n, and ϵ_b. For a reference model, we set $\alpha_{\rm acc} = 0.1$, $\epsilon_e = 0.3$, $\epsilon_n = 0.14$, and $\epsilon_b = 10^{-3}$. We compare the results to four pairs of models, where we increase and decrease each of the four parameters individually (see Tab. 1 for a list of models). In all cases, the power-law index of the non-thermal electrons was set to $q = 2.2$.

The synchrotron emission then follows directly from the settings for the magnetic field. We represent the seed for IC scattering by a simple model for the cosmic microwave background (CMB), viz. a field of photons of temperature $T_{\rm IC;0} = 2.7$ K with a uniform energy density of $u_{\rm IC;0} = 1\,{\rm eV/cm^3}$.

We show the spectral energy distribution of the radiation emitted by the shock-accelerated electrons at four different times in Fig. 1. Synchrotron radiation dominates the total radiative output at low energies with a broad peak in the range of UV to X-ray energies. The spectral indices and the cutoff frequencies of both components of the emission show little evolution with time, and consequently the spectra at different times have rather similar shapes. We find, on the other hand, considerable differences in the luminosities with time. The synchrotron radiation increases from $t = 300\,{\rm yr}$ and is greatest at $t = 600\,{\rm yr}$, be-

fore it gradually decreases again. For times $t = 600\,\mathrm{yr}$ and $t = 900\,\mathrm{yr}$, our results agree very well with the radio observations. For all times, the ASCA data lie in the steeply declining part of the synchrotron spectrum. The IC contribution is, in contrast to synchrotron, increasing steadily throughout the entire simulation time, though the brightening seems to slow down as we go from $t = 900\,\mathrm{yr}$ to $t = 1200\,\mathrm{yr}$. During this period, our results roughly match the observational data points. The main discrepancy is that our models do not reproduce the rather broad shape of the observed IC maximum. Assuming a thermal distribution of CMB seed photons rather than the monochromatic spectrum we used might bring our results closer to the observations.

We investigate the evolving appearance of the SNR in the series of emission maps presented in Fig. 2. Before hitting the four major clouds (*top* panels), the expanding shock wave maintains its ellipsoidal shape, and consequently the observational display of the SNR at low and high photon energies is dominated by the limb-brightened shock wave. The most prominent features are located at the shock wave along the semi-major axis of the ejecta. The non-thermal particles cool rather rapidly, and, hence, the interior regions of the SNR behind the shock wave remain dark. A few bright spots in the interior of the SNR indicate the positions of small clouds already hit by the shock wave. At a later time (*bottom* panels), the shock wave has already crossed the four main clouds, which now show up as additional emitters, in particular in the X-ray band. This enhanced emission reflects the rather high particle density and pressure at the shock-heated cloud surface as well as the reduced velocities in the flow hitting the cloud, where the fluid remains trapped for a fairly long time, thus reducing the adiabatic cooling of the non-thermal electrons.

We compare the results of the eight additional models in which we vary one input parameter at a time in Fig. 3. Lines of the same colour belong to the same pair of models, in which one parameter is either increased (dashed lines) or decreased (dash-triple-dotted lines) w.r.t. the reference model. The spectra, all taken at the same time, $t = 900\,\mathrm{yr}$, indicate how the choice of input physics affects the results:

- The acceleration parameter, α_{acc} (blue lines), by virtue of setting the maximum Lorentz factor of the electrons, strongly modifies the cutoff frequencies of both synchrotron and IC emission. Changing the value by one order of magnitude to higher ($\alpha_{\mathrm{acc}} = 1$) or lower ($\alpha_{\mathrm{acc}} = 0.01$) values reduces or increases the cutoff energies by approximately two orders of magnitude, but leaves the rising parts of the spectrum basically unchanged. In particular, both spectra still go through the radio data points.

- The parameter ϵ_e (green lines) setting the total fraction of the energy that goes into non-thermal particles is directly reflected in the normalisation of the spectra at all photon energies. It does, on the other hand, not have any impact on the high-energy cutoff. Both spectra with higher and lower values match the data considerably worse than our reference simulation does.

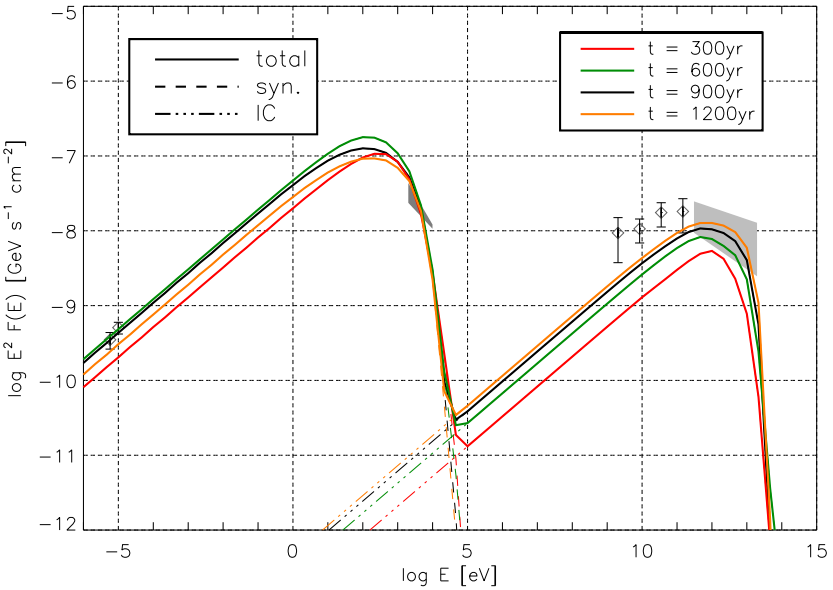

Figure 1: Broadband SED of our reference model for different times, distinguished by line colour. The total emission and the synchrotron and IC contributions are displayed by solid, dashed, and dash-dot-dot-dotted lines, respectively. For comparison, we include observations for the Vela Jr. SNR in radio (data points to the left; Duncan and Green, 2000), X-ray (*ASCA* GIS; shaded region around 2 keV; Aharonian et al., 2007), *Fermi*-LAT (data points in the GeV range; Tanaka et al., 2011), and *HESS* (shaded region to the right; Aharonian et al., 2007).

- The number fraction of accelerated electron, ϵ_n (red lines), has a comparably little influence on the spectra. The effect of lowering or rising its value has the opposite effect of lowering or rising ϵ_e: distributing the same amount of energy among more or less accelerated electrons leads to slightly lower or higher spectral power, respectively.

- The magnetisation of the medium, ϵ_b (orange lines), affects the spectra in a more complex way than the other three parameters. The magnetic field plays a role in setting the maximum energy of the electrons, and, most importantly, it directly determines the synchrotron losses. Stronger magnetic field ($\epsilon_b = 10^{-2}$) translates into a brighter synchrotron emission. Consequently, the electrons cool faster, which leads to a much weaker IC emission, in particular at high energies. Setting $\epsilon_b = 10^{-4}$ has the opposite effect: the electrons lose less energy due to synchrotron radiation and, therefore, emit stronger in the IC bands.

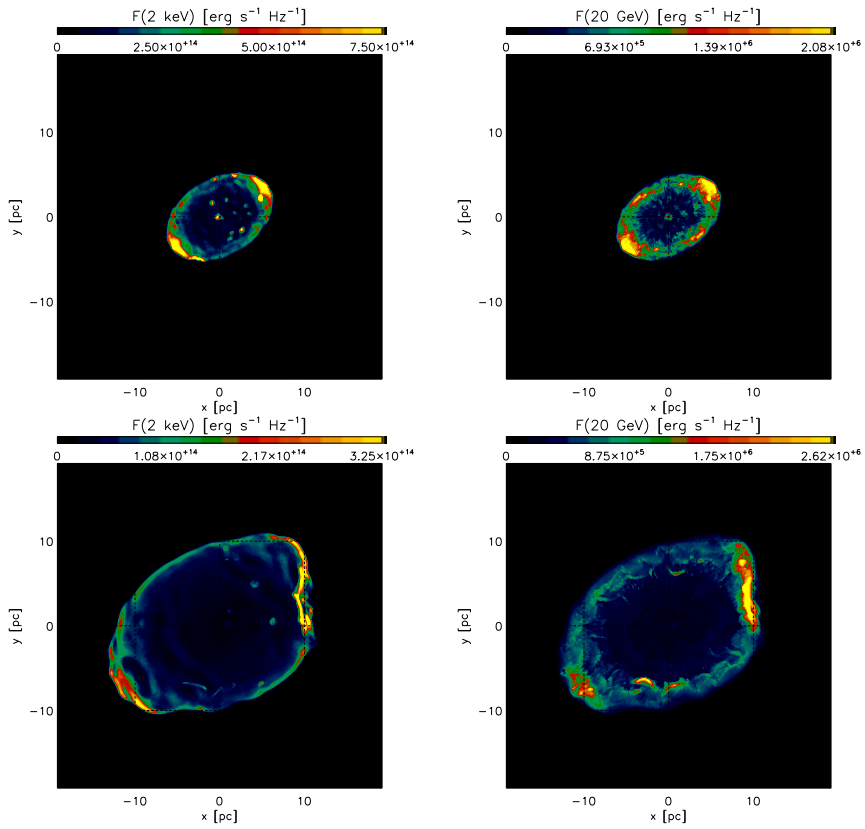

Figure 2: Emission maps in the X-ray (*left*) and GeV (*right*) bands at $t = 300\,\mathrm{yr}$ (*top*) and $t = 900\,\mathrm{yr}$ (*bottom*).

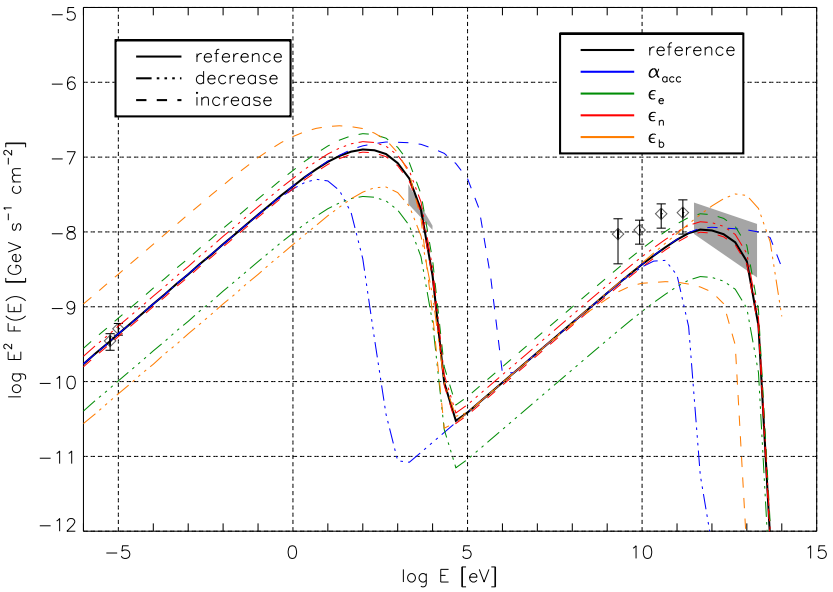

Figure 3: Comparison of the models with variations of the input parameters to the reference model (solid black line). The lines show the total emission at $t = 900\,\mathrm{yr}$ for each model. For each parameter, we computed a model with increased (dash-triple-dotted line) and a model with decreased (dashed line) value. Line colours distinguish between the four parameters (see also Tab. 1).

4. Summary and conclusions

Explaining the radiation observed in many galactic SNRs, characterised by non-thermal emission across a very broad band of photon energies as well as by a complex geometry, requires an approach combining multi-dimensional hydrodynamical simulations and a detailed modelling of the non-thermal radiation processes. To this end, we have adapted the methods used previously for computing the non-thermal emission of relativistic outflows to the situation of multi-dimensional non-relativistic SNRs expanding into a clumpy ISM.

A fraction of the electrons in the gas are accelerated to extremely relativistic energies when the shock wave passes across a fluid element and they subsequently emit synchrotron and inverse-Compton radiation. We apply a simple post-processing tool, *SPEVita*, based on the relativistic code SPEV Mimica et al. (2004). We follow the evolution of Lagrangian tracer particles advected with the flow. Upon passage of the shock wave, we set up a power-law distribution of the electrons. Starting from these initial states, we evolve the distribution taking into account adiabatic compression/expansion by the flow and energy losses due to synchrotron and IC radiation. We finally compute the detailed spectra of these two radiative processes by integrating the corresponding emissivities for all tracer particles. From these, we can straightforwardly obtain, e.g. spectra or two-dimensional emission maps.

Our method is less elaborate than, e.g. the scheme of Ellison et al. (2007); Patnaude et al. (2009); Lee et al. (2013) treating diffusive shock acceleration self-consistently. Therefore, as a first main step, we assessed its applicability in SNR models by computing a small set of emission models based on the same hydrodynamical simulation and varying some of the free parameters of the physics of non-thermal particles and their emission. We selected one of the three-dimensional simulations by Obergaulinger et al. (2014), consisting of an energetic bipolar explosion expanding into an ISM containing several large clouds. Although this particular hydrodynamical model was designed as a possible scenario for the observational appearance of SNR RX J0852.0-4622 (Vela Jr.), we do not intend to match the observational data of this or any other individual SNR here. We do, however, try to roughly reproduce the main features characteristic of most SNR.

The results of this first set of models show a reasonable quantitative agreement with the data of the Vela Jr. SNR. In particular, we clearly find the broad-band non-thermal emission with peaks in the UV-to-X-ray and GeV-to-TeV energies, produced by synchrotron and inverse-Compton scattering, with fluxes that are of the right order of magnitude. Geometrically, the emission is dominated by the immediate post-shock region. In addition, large clouds hit by the shock wave, can show up prominently, in particular in soft X-ray bands, after the shock wave has swept across them.

Instead of using different hydrodynamic models, we varied the parameters that govern our model for the acceleration and emission of non-thermal electrons, viz. the acceleration efficiencies, the relative energy and number densities of the accelerated particlces, and the magnetisation. Most of these changes

yield a significantly worse agreement with the observational data, which suggests that we might use future, more detailed models to constrain their likely values in SNRs, in particular if the remaining potential degeneracies can be reduced by complimentary observations, e.g., of the magnetic field in the vicinity of the explosion.

Having found a qualitative agreement between models and general observational features of SNRs, we plan to extend the present analysis by considering a wider range of physical parameters for the acceleration and emission processes and apply it to a larger set of (magneto-)hydrodynamical simulations in order to investigate the observational consequences of different sources for asymmetries in SNRs.

5. Acknowledgements

We thank Ewald Müller for stimulating discussions. AFI was partially supported through the Grant of RF "11.G34.31.0076". MO, PM, and MAA acknowledge support from the European Research Council (grant CAMAP-259276), and from the Spanish Ministerio de Ciencia e Innovación (grant AYA2013-40979-P *Astrofísica Relativista Computacional*) and from the Valencian Conselleria d'Educaciò (PROMETEO-2009-103).

References

Aharonian, F., Akhperjanian, A. G., Bazer-Bachi, A. R., Beilicke, M., Benbow, W., Berge, D., Bernlöhr, K., Boisson, C., Bolz, O., Borrel, V., Braun, I., Brown, A. M., Bühler, R., Büsching, I., Carrigan, S., Chadwick, P. M., Chounet, L.-M., Coignet, G., Cornils, R., Costamante, L., Degrange, B., Dickinson, H. J., Djannati-Ataï, A., Drury, L. O., Dubus, G., Egberts, K., Emmanoulopoulos, D., Espigat, P., Feinstein, F., Ferrero, E., Fiasson, A., Filipovic, M. D., Fontaine, G., Fukui, Y., Funk, S., Funk, S., Füßling, M., Gallant, Y. A., Giebels, B., Glicenstein, J. F., Goret, P., Hadjichristidis, C., Hauser, D., Hauser, M., Heinzelmann, G., Henri, G., Hermann, G., Hinton, J. A., Hiraga, J. S., Hoffmann, A., Hofmann, W., Holleran, M., Hoppe, S., Horns, D., Ishisaki, Y., Jacholkowska, A., de Jager, O. C., Kendziorra, E., Kerschhaggl, M., Khélifi, B., Komin, N., Konopelko, A., Kosack, K., Lamanna, G., Latham, I. J., Le Gallou, R., Lemière, A., Lemoine-Goumard, M., Lohse, T., Martin, J. M., Martineau-Huynh, O., Marcowith, A., Masterson, C., Maurin, G., McComb, T. J. L., Moulin, E., Moriguchi, Y., de Naurois, M., Nedbal, D., Nolan, S. J., Noutsos, A., Orford, K. J., Osborne, J. L., Ouchrif, M., Panter, M., Pelletier, G., Pita, S., Pühlhofer, G., Punch, M., Ranchon, S., Raubenheimer, B. C., Raue, M., Rayner, S. M., Reimer, A., Ripken, J., Rob, L., Rolland, L., Rosier-Lees, S., Rowell, G., Sahakian, V., Santangelo, A., Saugé, L., Schlenker, S., Schlickeiser, R., Schröder, R., Schwanke, U., Schwarzburg, S., Schwemmer, S., Shalchi, A., Sol, H., Spangler, D., Spanier, F., Steenkamp, R., Stegmann, C., Superina, G., Tam, P. H.,

Tavernet, J.-P., Terrier, R., Tluczykont, M., van Eldik, C., Vasileiadis, G., Venter, C., Vialle, J. P., Vincent, P., Völk, H. J., Wagner, S. J., Ward, M., #may# 2007. H.E.S.S. Observations of the Supernova Remnant RX J0852.0-4622: Shell-Type Morphology and Spectrum of a Widely Extended Very High Energy Gamma-Ray Source. ApJ661, 236–249.

Böttcher, A., Reimer, A., Jan. 2012. Relativistic Jets from Active Galactic Nuclei. Wiley, New York, Ch. 3. Radiation Processes, pp. 39–80.

Chevalier, R. A., Imamura, J. N., Oct. 1982. Linear analysis of an oscillatory instability of radiative shock waves. ApJ261, 543–549.

de Jager, O. C., Harding, A. K., Sep. 1992. The expected high-energy to ultra-high-energy gamma-ray spectrum of the Crab Nebula. ApJ396, 161–172.

Duncan, A. R., Green, D. A., 2000. The supernova remnant RX J0852.0-4622: radio characteristics and implications for SNR statistics. A&A364, 732–740.

Ellison, D. C., Patnaude, D. J., Slane, P., Blasi, P., Gabici, S., 2007. Particle Acceleration in Supernova Remnants and the Production of Thermal and Nonthermal Radiation. ApJ661, 879–891.

Gould, R. J., Oct. 1965. High-Energy Photons from the Compton-Synchrotron Process in the Crab Nebula. Physical Review Letters 15, 577–579.

Iyudin, A. F., Aschenbach, V., Burwitz, V., Dennerl, K., Freyberg, M., Haberl, F., Filipovic, M., 2007. Multiwavelength Appearance of Vela Jr.: Is it up to Expectations? In: ESA Special Publication. Vol. 622 of ESA Special Publication. p. 91.

Kishishita, T., Hiraga, J., Uchiyama, Y., 2013. Nonthermal emission properties of the northwestern rim of supernova remnant RX J0852.0-4622. A&A551, A132.

Lee, S.-H., Slane, P. O., Ellison, D. C., Nagataki, S., Patnaude, D. J., 2013. A CR-hydro-NEI Model of Multi-wavelength Emission from the Vela Jr. Supernova Remnant (SNR RX J0852.0-4622). ApJ767, 20.

Mimica, P., Aloy, M.-A., Agudo, I., Martí, J. M., Gómez, J. L., Miralles, J. A., 2009. Spectral Evolution of Superluminal Components in Parsec-Scale Jets. ApJ696, 1142–1163.

Mimica, P., Aloy, M. A., Müller, E., Brinkmann, W., 2004. Synthetic X-ray light curves of BL Lacs from relativistic hydrodynamic simulations. A&A418, 947–958.

Mimica, P., Giannios, D., Aloy, M. A., 2010. Multiwavelength afterglow light curves from magnetized gamma-ray burst flows. MNRAS407, 2501–2510.

Obergaulinger, M., Iyudin, A. F., Müller, E., Smoot, G. F., 2014. Hydrodynamic simulations of the interaction of supernova shock waves with a clumpy environment: the case of the RX J0852.0-4622 (Vela Jr) supernova remnant. MNRAS437, 976–993.

Orlando, S., Bocchino, F., Peres, G., Reale, F., Plewa, T., Rosner, R., Oct. 2006. Crushing of interstellar gas clouds in supernova remnants. II. X-ray emission. A&A457, 545–552.

Orlando, S., Peres, G., Reale, F., Bocchino, F., Rosner, R., Plewa, T., Siegel, A., Dec. 2005. Crushing of interstellar gas clouds in supernova remnants. I. The role of thermal conduction and radiative losses. A&A444, 505–519.

Orlando, S., Petruk, O., Bocchino, F., Miceli, M., Feb. 2011. Effects of non-uniform interstellar magnetic field on synchrotron X-ray and inverse-Compton γ-ray morphology of supernova remnants. A&A526, A129.

Patnaude, D. J., Ellison, D. C., Slane, P., 2009. The Role of Diffusive Shock Acceleration on Nonequilibrium Ionization in Supernova Remnants. ApJ696, 1956–1963.

Reynolds, S. P., 2008. Supernova Remnants at High Energy. ARA&A46, 89–126.

Slane, P., Hughes, J. P., Edgar, R. J., Plucinsky, P. P., Miyata, E., Tsunemi, H., Aschenbach, B., 2001. RX J0852.0-4622: Another Nonthermal Shell-Type Supernova Remnant (G266.2-1.2). ApJ548, 814–819.

Tanaka, T., Allafort, A., Ballet, J., Funk, S., Giordano, F., Hewitt, J., Lemoine-Goumard, M., Tajima, H., Tibolla, O., Uchiyama, Y., 2011. Gamma-Ray Observations of the Supernova Remnant RX J0852.0-4622 with the Fermi Large Area Telescope. ApJ740, L51.

Zdziarski, A. A., Jun. 1986. On the origin of the infrared and X-ray continua of active galactic nuclei. ApJ305, 45–56.